[3]W. Cochran, Acta Cryst. 9, 259 (1956).
[4]W. Cochran and G. Kartha, Acta Cryst. 9, 941 (1956); 9, 944 (1956).
[5]B. Borie, Acta Cryst. 10, 89 (1957); 12, 280 (1959).
[6]D. T. Keating, J. Phys. Chem. Solids 29, 771 (1968).
[7]C. R. Hall, J. Phys. Chem. Solids 30, 919 (1969).
[8]M. A. Krivoglaz *et al.*, Phys. Metals Metallog. 7, No. 5, 650 (1959); 9, No. 5, 641 (1960); 10, No. 2, 169 (1960); 12, No. 4, 465 (1961).
[9]M. A. Krivoglaz, *Theory of X-Ray and Thermal Neutron Scattering by Real Crystals* (Plenum, New York, 1969).
[10]M. A. Krivoglaz and K. P. Ryaboshapka, Phys. Metals Metallog. 16, No. 5, 641 (1963).
[11]S. R. Austerman and K. T. Miller, Phys. Status Solidi 11, 241 (1965).
[12]R. Collela and A. Merlini, Phys. Status Solidi 14, 81 (1966).
[13]H. Peisl, H. Spalt, and W. Waidelich, Phys. Status Solidi 23, K75 (1967).
[14]T. O. Baldwin, F. A. Sherrill, and F. W. Young, Jr., J. Appl. Phys. 39, 1541 (1968).
[15]J. E. Thomas, T. O. Baldwin, and P. H. Dederichs, Phys. Rev. B 3, 1167 (1971).
[16]H. Spalt, Z. Angew. Phys. 29, 269 (1970).
[17]P. H. Dederichs, Phys. Rev. B 1, 1306 (1970).
[18]A. Seeger and M. Ruhlë, Ann. Phys. (Leipzig) 11, 216 (1963), and references given therein.
[19]A. R. Stokes and A. J. C. Wilson, Proc. Phys. Soc. (London) 56, 174 (1944).
[20]H. Trinkhaus, thesis (Technische Hochschule Darmstadt, 1969) (unpublished).
[21]H. Trinkhaus, H. Spalt, and H. Peisl, Phys. Status Solidi 2, K97 (1970).
[22]M. Wilkens, Phys. Status Solidi 2, 692 (1962); 2, 1508 (1962); 3, 1718 (1963).
[23]A. J. C. Wilson, Proc. Roy. Soc. (London) 80, 286 (1962); 81, 41 (1963).

PHYSICAL REVIEW B VOLUME 4, NUMBER 4 15 AUGUST 1971

Ultrasonic Attenuation in Aluminum†

K. C. Hepfer* and J. A. Rayne
Carnegie-Mellon University, Pittsburgh, Pennsylvania 15213
(Received 26 March 1971)

The normal-state ultrasonic attenuation of longitudinal waves propagating along the principal symmetry directions in aluminum has been measured over a wide range of ql, where q is the phonon wave number and l is the electron mean free path. The usual quadratic frequency behavior at low ql and linear frequency behavior at high ql is observed for the electronic attenuation. At high ql the limiting values of attenuation divided by frequency are found to be strongly anisotropic and not in agreement with the free-electron prediction. Calculations assuming an isotropic deformation parameter with a pseudopotential representation of the Fermi surface show strong anisotropy, but the agreement with experiment is not good. From the pseudopotential Fermi surface generalized to include the effects of static strain, the anisotropy of the deformation tensor has been calculated. Using this model of the deformation, good agreement is achieved not only with the ultrasonic data but also with area changes observed from de Haas–van Alphen measurements under hydrostatic pressure.

I. INTRODUCTION

Ultrasonic waves propagating in a high-purity metal at low temperatures experience a large attenuation owing to the electrons in the metal. A general theory[1] expresses the electronic attenuation in terms of several integrals over the Fermi surface involving the wave number q, the electron mean free path l, and the deformation properties of the Fermi surface under static strain. At higher frequencies, where the product ql becomes much greater than 1, the attenuation becomes linear in the frequency and independent of electron mean free path. For longitudinal waves, the major contribution to the attenuation comes from those areas of the Fermi surface where the normal to the surface is nearly perpendicular to the direction of the propagation; these regions are known as effective zones. Since the longitudinal ultrasonic attenuation at high ql in a metal depends only upon the shape of its Fermi surface and upon the deformation properties along the effective zones, measurements in several different directions at high ql should provide information about the magnitude and anisotropy of the deformation tensor.

In addition to the availability of high-purity single crystals, aluminum is a desirable metal for such an investigation because its Fermi surface can be accurately expressed in terms of a pseudopotential model based on de Haas–van Alphen (dHvA) measurements.[2] Previous measurements[3–7] in aluminum have generally been over a limited range of ql and the high-frequency limiting values have not been in agreement. In this paper, measurements of longitudinal ultrasonic attenuation in aluminum over a wide range of ql are reported and the results

measurements does not rule out dislocation attenuation as an explanation of the observed temperature dependence of the background attenuation.

Although the necessary parameters are not known well enough to make even a qualitative theoretical estimate of the temperature dependence of the dislocation attenuation, some information about the temperature dependence of the background attenuation can be obtained by careful examination of the experimental curves of attenuation vs temperature. Below about 5 °K, the electronic mean free path has a constant impurity-limited value and hence the electronic attenuation must also be constant. As the temperature rises from about 5 to 10 °K, the electronic mean free path is expected to slightly decrease from its maximum value, and in this region of high ql one would strongly expect the electronic attenuation to remain constant or slightly decrease with increasing temperature. Since the electronic attenuation is expected to remain constant or decrease slightly from 0 to about 10 °K, the observed increase of the experimental attenuation in this region (see Fig. 2) must be due to an equal or greater increase in the background attenuation over this temperature range.

At high temperature where the electronic attenuation is expected to be small, an estimate of the background attenuation has been obtained by the following method: The electrical resistivity of the sample at high temperature is assumed to follow a Block-Grüneisen form[13] and a temperature-dependent mean free path is obtained from the resistivity. With the electron mean free path known, the electronic attenuation is then calculated using the free-electron theory.[14] Finally, the estimated electronic attenuation is subtracted from the measured attenuation to get the estimated background attenuation as shown by the squares in Fig. 2. Although this approximation of the electronic attenuation at high temperature is certainly not exact, it is probably not in error by more than 50%.

In the intermediate temperature region the experimental attenuation curve can furnish no information about the background attenuation, so in this region a smooth curve is assumed to connect the slowly varying high-temperature behavior with the more rapidly varying low-temperature behavior. A curve, such as is shown by the dashed line on Fig. 2, is taken as the best estimate of the background attenuation. The total uncertainty in the background attenuation at 0 °K is assumed to be about seven times as large as the difference between the experimental attenuation at 0 °K and the attenuation at the peak of the experimental curve. It is felt that this error estimate would cover almost any possible form for the temperature dependence of the background attenuation.

Table III gives the resulting values of electronic attenuation as a function of frequency and propagation direction for the samples of highest purity. Figures 3–5 show graphs of α/f vs frequency for all the samples and frequencies measured (α here refers to the electronic attenuation at 0 °K). For each propagation direction, the frequency values for the higher-purity samples have been multiplied by a constant scaling factor, so that all the data lie on a smooth curve. The scaling factor for each sample should then equal the ratio of the electron mean free path in that sample l to the electron mean free path in the lowest-purity sample l_0,

TABLE III. Measured electronic attenuation as a function of frequency and propagation direction for high-purity aluminum.

Propagation direction	Sample No.	Frequency (MHz)	Attenuation (dB cm^{-1})
[100]	1	30.7	7.9 ± 1.1
		50.6	15.9 ± 0.8
		70.8	$24.3 \pm {2.5 \atop 5.0}$
		90.4	29.7 ± 4.0
		151.0	53.9 ± 6.0
		211.0	74.8 ± 12
		273.0	101 ± 12
		334.5	125 ± 12
		392.0	146 ± 20
	2	11.3	2.2 ± 0.2
		15.6	3.5 ± 0.6
		25.9	7.0 ± 0.6
		30.0	9.0 ± 0.5
		50.8	17.5 ± 1.3
		70.6	24.3 ± 1.4
		89.7	31.8 ± 1.5
		111.1	39.5 ± 1.5
		131.0	47.0 ± 2.0
		149.9	55.1 ± 4.0
[110]	3	15.6	2.5 ± 0.3
		30.6	9.1 ± 0.6
		35.4	10.5 ± 0.4
		55.4	20.2 ± 1.0
		91.3	40 ± 2
		151.0	69 ± 3
		213.5	101 ± 4
		271.0	132 ± 5
[111]	4	90.0	21 ± 5
		151.8	34 ± 3
		270.2	62 ± 5
		332.0	77 ± 7
		513.5	121 ± 20
[111]	5	11.3	1.69 ± 0.04
		30.7	7.8 ± 1.0
		31.0	7.1 ± 0.2
		50.9	12.9 ± 0.3
		90.0	25 ± 1
		153.3	42 ± 3
		211.0	58 ± 4

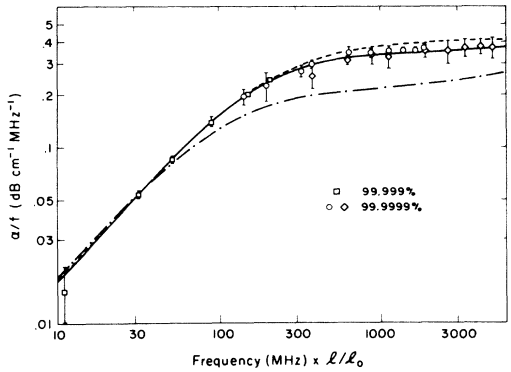

FIG. 3. Frequency and mean free path dependence of α/f for longitudinal waves propagating along [100] in aluminum. Dashed curve represents the predicted free-electron behavior, dot-dashed curve represents the prediction of the 4-OPW Fermi surface with an isotropic deformation, and the solid curve represents the prediction of the 4-OPW Fermi surface with the anisotropic deformation model described in the text.

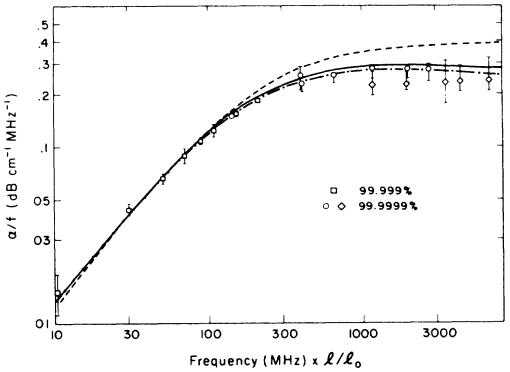

FIG. 5. Frequency and mean free path dependence of α/f for longitudinal waves propagating along [111] in aluminum. Dashed curve represents the predicted free-electron behavior, dot-dashed curve represents the prediction of the 4-OPW Fermi surface with an isotropic deformation, and solid curve represents the prediction of the 4-OPW Fermi surface with the anisotropic deformation model described in the text.

as given in Table I. In all cases this requirement is satisfied to within the experimental uncertainty. The modified frequency scale ($f \times l/l_0$) is proportional to ql with the proportionality constant being $2\pi l_0/v_s$, where v_s is the velocity of sound. The points on these three graphs summarize all the experimental data in a form which allows direct comparison with the theoretical calculations of electronic attenuation.

The quantity of greatest theoretical interest is the limiting value of α/f as $ql \to \infty$, since this quantity can be related to the geometry and deformation characteristics of a limited region of the Fermi surface. Table IV summarizes the measured values of α/f for $ql \gg 1$ and gives a comparison with previous measurements in aluminum. The latter have demonstrated the anisotropy of α/f at high ql, but there has been considerable disagreement as to actual values. It is believed that the present work gives the most reliable directly measured data covering a wide range of ql. More recent experiments[15] on very-high-purity aluminum with a resistance ratio of 14500 have confirmed the results for [100] propagation and have extended the value of ql to beyond 100. A meaningful comparison of the present data with theory is thus presumably justified.

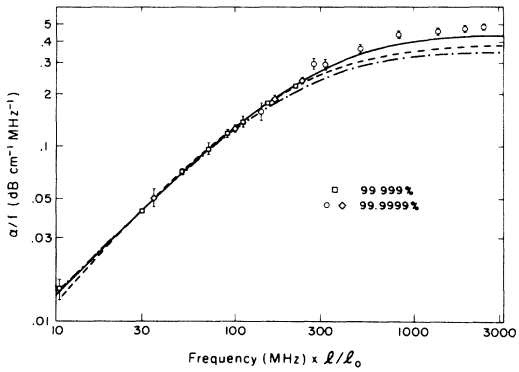

FIG. 4. Frequency and mean free path dependence of α/f for longitudinal waves propagating along [110] in aluminum. Dashed curve represents the predicted free-electron behavior. Dot-dashed curve represents the prediction of the 4-OPW Fermi surface with an isotropic deformation, and solid curve represents prediction of the 4-OPW Fermi surface with the anisotropic deformation model described in the text.

III. THEORY

A. Electronic Attenuation

According to the general theory of ultrasonic attenuation in metals,[1] the attenuation of a longitudinal wave propagating along a direction of high symmetry is given by

$$\alpha = (\hbar q/4\pi^3 \rho v_s)(A + B^2/C) , \tag{1}$$

where A, B, and C are integrals over the Fermi surface, viz.,

$$A = \int_{FS} \frac{\mathfrak{D}^2 a\, dS}{1 + a^2 \cos^2\varphi} , \quad B = \int_{FS} \frac{\mathfrak{D}\, dS}{1 + a^2 \cos^2\varphi} , \quad C = \int_{FS} \frac{a \cos^2\varphi\, dS}{1 + a^2 \cos^2\varphi} . \tag{2}$$

In these equations q is the wave number of the ultrasonic wave, ρ is the density of the metal, v_s

TABLE IV. Values of α/f at high ql as reported by various sources.

Propagation direction	α/f for $ql \gg 1$					
	D[a]	B[b]	F[c]	B[d]	T[e]	Present work[f]
[100]	0.6 ± 0.1	0.5	0.364	0.4 ± 0.03	0.5 ± 0.05	0.36 ± 0.04
[110]	0.8 ± 0.2	0.62	···	0.62 ± 0.03	0.54 ± 0.05	0.48 ± 0.03
[111]	···	0.3	···	0.33 ± 0.03	0.34 ± 0.03	0.27 ± 0.03

[a]See Ref. 3. Values of $\alpha_n - \alpha_s$ extrapolated to 0 °K. Maximum ql about 10 and 4 for [100] and [110] propagation, respectively.

[b]See Ref. 4. Indirect method involving magnetic field dependence of attenuation. Maximum ql about 20, but quoted values extrapolated to infinite ql.

[c]See Ref. 5. Value of $\alpha_n - \alpha_s$ at 9.4 GHz extrapolated to 0 °K. Sample only approximately oriented, although ql probably in excess of 100.

[d]See Ref. 6. Values of $\alpha_n - \alpha_s$ extrapolated to 0 °K with maximum ql of about 60.

[e]See Ref. 7. Values of α_n obtained indirectly by fitting superconducting attenuation to BCS theory with $\Delta = 1.75 k_B T_C$

[f]Values quoted are for $ql = 20$, the mean free path l being estimated from electrical resistivity.

is the velocity of sound, and a is the product ql, where l is the electron mean free path which is assumed to be impurity limited and isotropic. The angle between the direction of propagation Ox and the normal to the Fermi surface is denoted by φ, while $\mathfrak{D}$ is given by

$$\mathfrak{D} = K_x + k_x \cos\varphi, \tag{3}$$

where k_x is the component of the Fermi surface wave number in the direction of propagation, and K_x is the deformation parameter for static longitudinal strain along the propagation direction. (For a strain $\tilde{\omega}_x$, the Fermi surface will move normal to itself a distance $K_x \tilde{\omega}_x$.)

Charge conservation imposes one condition on the function K_x, in that the fractional change in the volume of the Fermi surface must be equal and opposite to the fractional change in the volume of the metal. This requirement gives the usual expression of charge conservation

$$\int_{FS} \mathfrak{D}\, dS = \int_{FS} (K_x + k_x \cos\varphi)\, dS = 0 . \tag{4}$$

If K_x is assumed to be isotropic or constant, then from Eq. (4),

$$K_x = -\int_{FS} k_x \cos\varphi\, dS / \int_{FS} dS . \tag{5}$$

Any part of the Fermi surface in contact with the Brillouin zone can be excluded from the integrals in Eqs. (4) and (5), since on the Brillouin zone it is always true that $K_x + k_x \cos\varphi = 0$.

For a free-electron sphere of radius k_F, $K_x = -\frac{1}{3} k_F$ and Eq. (1) can be evaluated to give

$$\alpha = (nm v_F / \rho v_s l)[a^2 \tan^{-1} a / 3(a - \tan^{-1} a) - 1] , \tag{6}$$

where n is the number of electrons per unit volume, v_F is the Fermi velocity, and m is the mass of the electron. When the Fermi surface is nonspherical, Eq. (1) is much more difficult to evaluate, but in the two limiting cases $a \ll 1$ and $a \gg 1$, the second term is unimportant and certain general features of the attenuation can be observed.

For $a \ll 1$, Eq. (1) reduces to

$$\alpha \approx (\hbar^2 / 4\pi^3 \rho v_s) q^2 \int_{FS} \mathfrak{D}^2 dS = \text{const} \times q^2 l , \tag{7}$$

so that the attenuation is proportional to the electron mean free path and the square of the wave number. For $a \gg 1$, the function $(1 + a^2 \cos^2\varphi)^{-1}$ becomes strongly peaked in $\cos\varphi$ with a width at half-maximum of $2/a$. To a rough approximation one can write

$$\alpha \approx \text{const} \times q \int_{BZ} K_x^2 a\, dS , \tag{8}$$

with the integration being taken over the so-called effective zone on the Fermi surface where $\cos\varphi \leq 1/a$. For many surfaces (no flat spots, cusps, or large changes in curvature) the area of the effective zone will be proportional to $1/a$ and the function α/q will approach a limiting value as a increases. This limiting value depends only on the geometry and deformation characteristics of the Fermi surface.

B. Pseudopotential Fermi-Surface Model

A 4-orthogonalized-plane-wave (4-OPW) pseudopotential Fermi-surface model for aluminum has been developed to fit dHvA data.[2] In this model, the valence-electron wave function is expanded in terms of normalized plane waves and the Fermi surface is defined by solutions to the secular determinant

$$\det(\langle \vec{k} + \vec{g} | T + V | \vec{k} + \vec{g}' \rangle - E_F \delta_{\vec{g}\vec{g}'}) = 0 , \tag{9}$$

where T is the kinetic energy operator, V is the weak-pseudopotentia operator, and $\vec{g}$ is the position of a reciprocal-lattice point. The success of the nearly-free-electron model of the aluminum Fermi surface[16,17] would indicate that the pertur-

bation of the energy bands is only significant near Bragg-reflection planes. Thus, the significant terms in the above determinant will be for values of $\vec{g}$ and $\vec{g}'$ where the plane bisecting the line $\vec{g}$-$\vec{g}'$ intersects the Fermi surface. For the $\frac{1}{24}$th of the Fermi surface bounded by the directions [100], [111], and [11$\bar{1}$], the planes (111), (11$\bar{1}$), and (200) will intersect the Fermi surface. To a good approximation, then, the Fermi surface can be defined by solutions to the fourth-order secular determinant

$$\begin{vmatrix} T_0 & V_{111} & V_{111} & V_{200} \\ V_{111} & T_1 & V_{200} & V_{111} \\ V_{111} & V_{200} & T_2 & V_{111} \\ V_{200} & V_{111} & V_{111} & T_3 \end{vmatrix} = 0 \quad , \tag{10}$$

where

$$\begin{aligned} T_0 &= \vec{k}^2 - E_F \quad , \\ T_1 &= [\vec{k} - (1, 1, 1)]^2 - E_F \, , \\ T_2 &= [\vec{k} - (1, 1, \bar{1})]^2 - E_F \quad , \\ T_3 &= [\vec{k} - (2, 0, 0)]^2 - E_F \quad . \end{aligned} \tag{11}$$

The units of the above equations are chosen such that $2\pi/a = 1$ and $\hbar^2/2m = 1$. V_{111} and V_{200} are the first and second Fourier coefficients of the effective crystal potential, E_F is the Fermi energy, and the zero of energy is defined so that $V_{000} = 0$. If the determinant of Eq. (10) is expanded and simplified, the resulting fourth-order polynomial

$$\begin{aligned} &(T_0 T_3 - V_{200}^2)\,(T_1 T_2 - V_{200}^2) \\ &- V_{111}^2\,(T_0 + T_3 - 2V_{200})\,(T_1 + T_2 - 2V_{200}) = 0 \end{aligned} \tag{12}$$

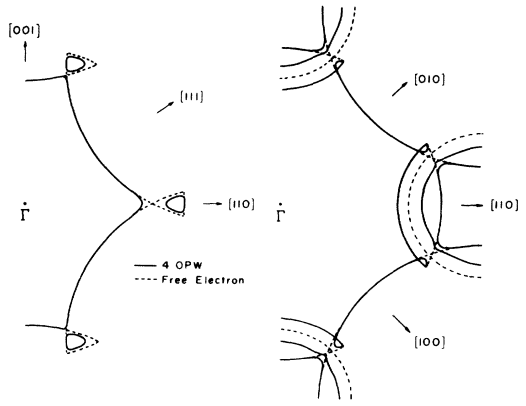

FIG. 6. Two central cross sections through the aluminum Fermi surface perpendicular to [1$\bar{1}$0] and [001]. Dashed and full curves show the predictions of the free electron and 4-OPW models, respectively.

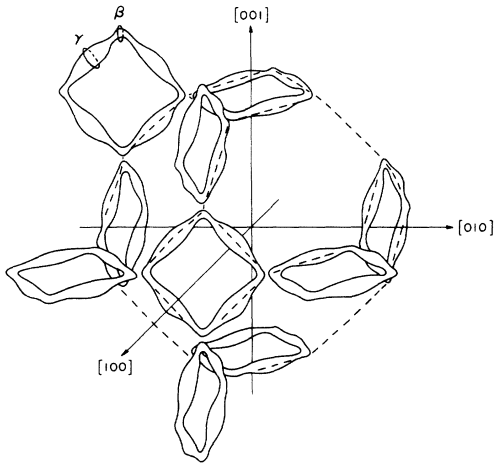

FIG. 7. Third-zone Fermi surface of aluminum in the repeated zone scheme. Brillouin zone is shown dashed and β and γ cross sections are shown for one of the arms.

is somewhat more convenient for computation. As written, the above equations define the $\frac{1}{24}$th of the Fermi surface bounded by the directions [100],

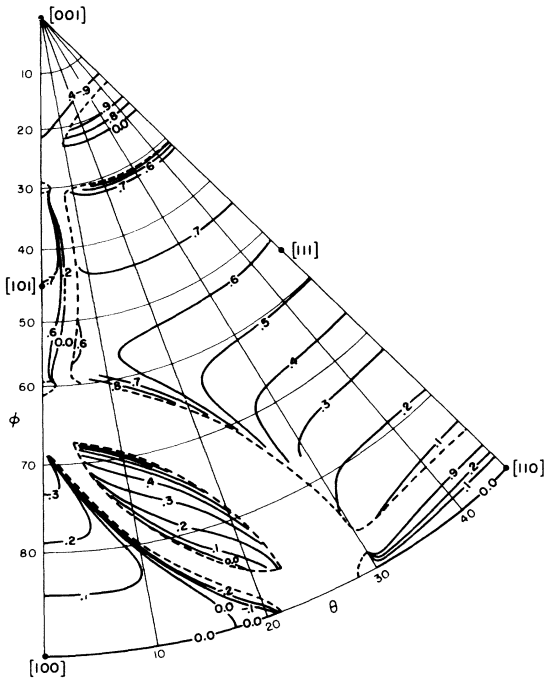

FIG. 8. Stereographic projection of curves of constant cosφ on the extended-zone Fermi surface of aluminum for [001] propagation, φ being the angle between the normal to the Fermi surface and the propagation direction. The pole of the stereographic projection is [001] and the intersection of the Fermi surface with the Brillouin zone is shown dashed. Angular coordinates are θ, ϕ, respectively.

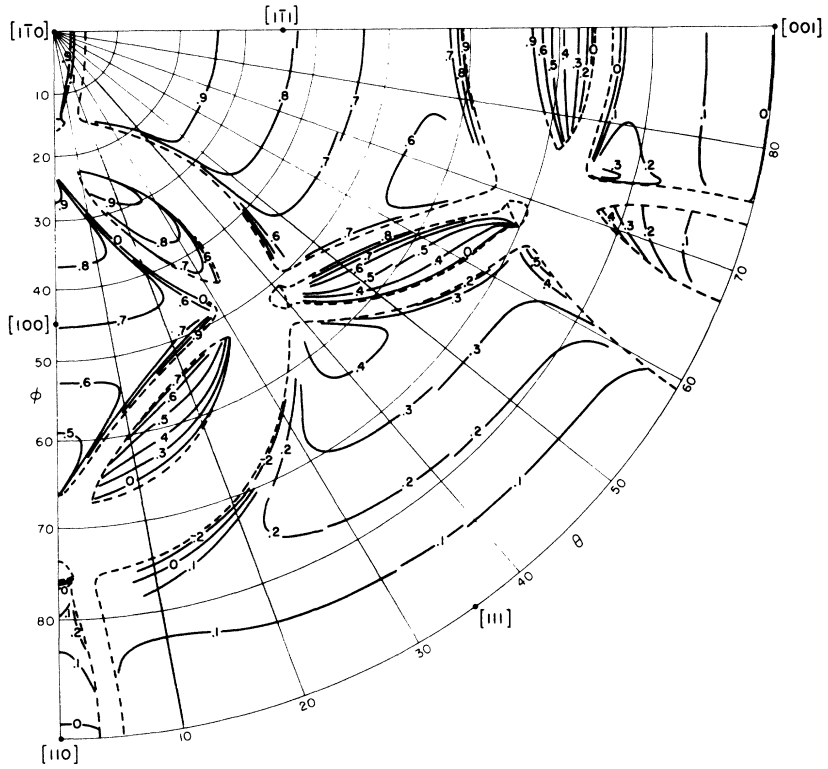

FIG. 9. Stereographic projection of curves of constant $\cos\varphi$ on the extended-zone Fermi surface of aluminum for [1$\bar{1}$0] propagation, φ being the angle between the normal to the Fermi surface and the propagation direction. The pole of the stereographic projection is [1$\bar{1}$0] and the intersection of the Fermi surface with the Brillouin zone is shown dashed. Discontinuous breaks in the contours are the result of truncating the secular determinant to order four. Angular coordinates are θ, ϕ, respectively.

[111], and [11$\bar{1}$], but because of symmetry only the $\frac{1}{48}$th bounded by directions [100], [111], and [110] is needed to completely define the Fermi surface.

This model has just three adjustable parameters: E_F, V_{111}, and V_{200}, which are adjusted to give the Fermi surface the correct volume and the correct shape. In the dimensionless units used, the parameters have the values $E_F = 1.264$, $V_{111} = 0.02642$, and $V_{200} = 0.08295$; in conventional units they are $E_F = 0.85605$, $V_{111} = 0.0179$, and $V_{200} = 0.0562$ Ry.[2] If V_{111} and V_{200} were both 0, all solutions to Eq. (12) would lie on spherical surfaces of radius $E_F^{1/2}$ centered at the reciprocal-lattice points (0, 0, 0), (1, 1, 1), (1, 1, $\bar{1}$), and (2, 0, 0) giving the so-called Harrison construction.[16] The effect of introducing V_{111} and V_{200} is to break up and distort the spherical surfaces near their regions of intersection. Figure 6 shows how the pseudopotential rounds off the sharp edges and corners of the free-electron second-zone surface but leaves the general shape intact. The effect of the pseudopotential on the free-electron third-zone "arms" is somewhat more pronounced, producing the noticeably smaller "arms" which are joined into "rings of four" as shown in Fig. 7. Figures 8–10 show stereographic projections giving the curves of constant $\cos\varphi$ on the model Fermi surface for propagation along [001], [1$\bar{1}$0], and [1$\bar{1}$1], respectively. In these figures the angular coordinates are represented by the angles θ, ϕ, respectively.

Some idea of the discrepancies still remaining in this model can be obtained by considering the symmetry required of the true Fermi surface. In particular, the boundary planes of the $\frac{1}{48}$th symmetry section [(001), (1$\bar{1}$0), and (01$\bar{1}$)] are all reflection planes and hence when the Fermi surface intersects one of these planes, the normal to the Fermi surface should lie in the plane. The normal to the model Fermi surface deviates from its symmetry-determined position by as much as 1 deg in some places and this lack of perfect symmetry can be traced directly to the truncation of the secular equation (10) to order four. The third-zone cross sections, which principally determine the parameters V_{111} and V_{200}, are known to within a few percent,[2] and hence the dimensions of the model surface may deviate from the true Fermi surface by several percent. Errors in the dimensions of the surface will not produce large effects on the calculated attenuation, but a 1-deg error in the normal to the surface will appreciably limit the accuracy of some of the calculations made in Sec. IV. Figure 9 clearly shows the effects produced by the truncation.

IV. CALCULATIONS AND RESULTS

A. Free-Electron Model

If Eq. (6) is evaluated using the physical constants of aluminum, the prediction of the free-electron

TABLE V. Comparison of theoretical and experimental values of α/f for longitudinal wave propagation in aluminum.[a]

Propagation direction	α/f (dB cm^{-1} MHz^{-1}) Free electron	Isotropic deformation	Anisotropic deformation	Expt
[100]	0.403	0.226	0.355	0.36 ± 0.04
[110]	0.386	0.350	0.435	0.48 ± 0.03
[111]	0.379	0.271	0.290	0.27 ± 0.03

[a]Values at $ql = 20$, q being phonon wave number and l the electron mean free path estimated from electrical resistivity.

model of ultrasonic attenuation is that

$$\alpha/f = \text{const} \times P(ql) \text{ dB cm}^{-1} \text{ MHz}^{-1} , \quad (13)$$

where the constant has the values 0.4237, 0.4052, and 0.3985 for propagation along [100], [110], and [111], respectively. The function $P(a)$ is given by

$$P(a) = (6/\pi)\,(1/a)\,[a^2 \tan^{-1}a/3(a - \tan^{-1}a) - 1], \quad (14)$$

and has the property that

$$P(a) = (8/5\pi)a = 0.509\,a , \quad a \ll 1$$
$$P(a) = 1 + [\tfrac{1}{2}\pi - (8/\pi)]/a = 1 - 0.976/a , \quad a \gg 1 . \quad (15)$$

The slight anisotropy of the attenuation in the free-electron model is due to the variation of the sound velocity with propagation direction.

For low-purity samples or low frequencies ($ql < 1$), the experimental data can be fitted quite well by the free-electron model, with samples of the same purity requiring about the same value of l. However, for the higher-purity samples at higher frequencies ($ql \gg 1$), the experimental data show a large anisotropy, which is not predicted at all by the free-electron theory. The discrepancies can be seen in Table V and in Figs. 3–5.

B. Isotropic Deformation Model

As shown by Figs. 6 and 7, some parts of the aluminum Fermi surface deviate significantly from the sphere of the free-electron model and it would be expected that this distortion would produce changes in the electronic contribution to the attenuation. In order to determine the magnitude of these changes, a computer program has been developed to calculate the longitudinal ultrasonic attenuation using the model Fermi surface and assuming an isotropic deformation. For the purpose of making the calculations, an extended-zone representation of the Fermi surface is used.

Equation (5) has been evaluated to give the isotropic deformation appropriate to the model Fermi surface, viz., $K_{iso} = -0.353(2\pi/a) = -0.314\,k_F$. Then, using this value for K_x, the attenuation has been calculated from Eq. (1) for propagation along the three principal symmetry directions and for about ten values of ql. Because of symmetry requirements, the relevant integrals only need to be taken over a part of the Fermi surface. For [001] propagation, the integrals can be taken over the $\frac{1}{16}$th of the Fermi surface bounded by the directions [001], [110], and [100] and the results multiplied by 16. For [1$\bar{1}$0] propagation, the integrals can be taken over the $\frac{1}{8}$th of the Fermi surface bounded by the directions [1$\bar{1}$0], [001], and [110] and the results multiplied by 8. Finally, for [1$\bar{1}$1] propagation, the $\frac{1}{12}$th bounded by the directions [1$\bar{1}$1], [111], and [11$\bar{1}$] can be used and the results multiplied by 12.

Because of the cubic symmetry of aluminum, $\frac{1}{48}$th of the Fermi surface is sufficient to completely define the shape of the entire Fermi surface. When doing numerical integration with a computer, it is much simpler to integrate over $\frac{1}{48}$th of the Fermi surface for several propagation directions rather than to integrate over several sections for one propagation direction. For example, for [001] propagation the $\frac{1}{48}$th bounded by [100], [111], and [110] is used and propagation is assumed along [001], [100], and [010]. A system of curvilinear coordinates is set up on the Fermi surface and at about 4000 points on the $\frac{1}{48}$th section the position and the normal to the Fermi surface are calculated. The integrals of Eqs. (2) and (5) are then approximated by summations over the 4000 points.

For $ql \gg 1$, the main contribution to the attenuation comes from that part of the Fermi surface where $\cos\varphi \lesssim 1/ql$. For some propagation directions, the line $\cos\varphi = 0$ should lie along the edge of the $\frac{1}{48}$th section of the Fermi surface used for the integration. Because of the lack of perfect symmetry in the model Fermi surface, the line $\cos\varphi = 0$ may lie slightly within or without the $\frac{1}{48}$th of the section and since the function $(1 + a^2\cos^2\varphi)^{-1}$ is peaked at $\cos\varphi = 0$, the calculated attenuation will be larger or smaller than it should be. Although a partial correction for the error has been made, reliable calculations of α/f vs ql for [110] propagation are limited to $ql < 50$ by this effect.

The results of the isotropic deformation model calculations are shown by the dot-dashed curves in Figures 3–5 and in Tables II and V. For $ql < 1$, the isotropic deformation model provides about as good a fit to the data as the free-electron model, but the value of l required to fit the low-ql data varies as much as 40% for different propagation directions in the same specimen (see Table II, sample No. 6). For $ql < 1$, the isotropic deformation model predicts a large anisotropy for the attenuation (see Table V), but the predictions are

not in agreement with experiment except for [111] propagation.

Although the isotropic deformation model does not adequately explain the measured attenuation, it does provide a clear picture of how the Fermi-surface shape affects the ultrasonic attenuation. When ql is large, only the effective zone on the Fermi surface where $\cos\varphi \gtrsim 1/ql$ contributes significantly to the attenuation. For a free-electron Fermi surface, $\varphi = \phi$, so the free-electron effective zone will be a uniform band centered about the line $\phi = 90°$. Reference to Fig. 8 shows that for [100] propagation with ql above about 2, the effective zone (and hence α/f) will be relatively smaller than the corresponding zone for the free-electron case. Near the point $\phi = 90°$ and $\theta = 17°$, there seems to be a flat spot on the Fermi surface where $\cos\varphi = 0$. This property implies that the area of the effective zone will approach a constant as $ql \to \infty$ and hence Eq. (8) will be proportional to $q^2 l$ as $ql \to \infty$. Thus, one would expect the function describing α/f to increase linearly with frequency for very high ql in contrast to the usual saturation behavior.

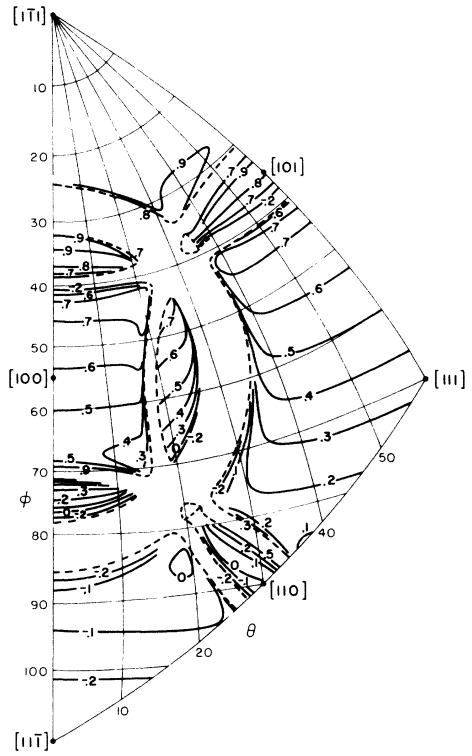

FIG. 10. Stereographic projection of curves of constant $\cos\varphi$ on the extended-zone Fermi surface of aluminum for [1$\bar{1}$1] propagation, φ being the angle between the normal to the Fermi surface and the propagation direction. Pole of the stereographic projection is [100] and the intersection of the Fermi surface with the Brillouin zone is shown dashed. Angular coordinates are θ, ϕ, respectively.

From Fig. 9 it can be seen that, for [1$\bar{1}$0] propagation with ql greater than about 5, the effective zone is only slightly smaller than the corresponding zone for the free-electron surface. Hence α/f at high ql should be only slightly smaller than the free-electron prediction. For [1$\bar{1}$1] propagation, however, the situation is somewhat more difficult to analyze. With ql between about 2 and 5, Fig. 10 shows that the effective zone is smaller than for the free-electron surface because of gaps in the model Fermi surface. At $ql = 10$ the effective zone is an irregular band near $\phi = 90°$, while for higher-ql values, it shrinks rapidly toward the region indicated by the zero contour, centered near $\phi = 85°$ and $\theta = 18°$. This rapid decrease in the effective zone produces a slow decrease in the function α/f as ql increases above about 10.

Another interesting effect on the attenuation is produced by the shape of the model Fermi surface near $\phi = 90°$ (Fig. 10). Since $\cos\varphi$ becomes increasingly negative on both sides of some line near $\phi = 90°$, the effect of shifting the propagation direction either slightly towards or away from [100] is to widen or narrow the effective zone. Because of this, relatively small shifts in the propagation direction could produce relatively large shifts in the attenuation at high ql. By shifting the propagation direction slightly in the computer program, it is estimated that a change in propagation from [1$\bar{1}$1] toward [100] would produce an increase in attenuation of about 15%/deg at $ql = 20$. Since the values of attenuation measured in the two high-purity [111] samples are not in good agreement (see Fig. 5), a careful check of the propagation directions was made using a high-accuracy Laue technique. The results are that sample No. 4 is oriented $\frac{1}{2}° \pm \frac{1}{4}°$ from [111] toward [110] (away from [100]) and sample No. 5 is oriented $\frac{1}{2}° \pm \frac{1}{4}°$ from [111] toward [100]. Therefore, most of the disagreement in α/f for the high-purity [111] samples can be explained by misorientation, producing the large effects described above.

C. Anisotropic Deformation Model

The results of Sec. IV B indicate that the deformation parameter of the aluminum Fermi surface must be anisotropic in order to explain the observed electronic attenuation. Because ultrasonic attenuation measurements can provide at best an rms average of the deformation parameter over some part of the Fermi surface, the experimental results are not very useful for determining a completely empirical model of the deformation. Rather, they are better suited for checking a model that has already been determined by theoretical or

other experimental information. Such an anisotropic model for the deformation has been developed by considering the effect of lattice strain on the pseudopotential representation of the Fermi surface.

In Sec. III, the $\frac{1}{48}$th of the Fermi surface bounded by the directions [100], [111], and [110] was defined by solutions to Eq. (10). If a very small linear strain is applied to the metal, then the same $\frac{1}{48}$th of the Fermi surface should be described by a similar equation, namely,

$$\begin{vmatrix} T_0' & V_{111}+\lambda_1 & V_{111}+\lambda_2 & V_{200}+\lambda_3 \\ V_{111}+\lambda_1 & T_1' & V_{200}+\lambda_4 & V_{111}+\lambda_5 \\ V_{111}+\lambda_2 & V_{200}+\lambda_4 & T_2' & V_{111}+\lambda_6 \\ V_{200}+\lambda_3 & V_{111}+\lambda_5 & V_{111}+\lambda_6 & T_3' \end{vmatrix} = 0 , \quad (16)$$

where

$$\begin{aligned} T_0' &= \vec{k}^2 - E_F - \delta , \\ T_1' &= [\vec{k} - (1,1,1) - \vec{\mu}_1]^2 - E_F - \delta , \\ T_2' &= [\vec{k} - (1,1,\bar{1}) - \vec{\mu}_2]^2 - E_F - \delta , \\ T_3' &= [\vec{k} - (2,0,0) - \vec{\mu}_3]^2 - E_F - \delta , \end{aligned} \quad (17)$$

and the λ's, $\vec{\mu}$'s, and δ's represent strain-dependent changes in the pseudopotential coefficients, reciprocal-lattice vectors, and Fermi energy, respectively. The units of the above equations and those which follow are chosen such that $2\pi/a = 1 = \hbar^2/2m$. If the quantities λ_i, $\vec{\mu}_i$, and δ can be expressed in terms of the strain, then the deformation parameter at a given point on the Fermi surface is just the normal distance measured from that point on the unstrained Fermi surface to the strained Fermi surface, divided by the magnitude of the strain.

In the work which follows, a positive strain is taken to mean a longitudinal compression of the real metal or a longitudinal dilation of the reciprocal lattice. Let $\vec{\epsilon}$ be a small vector in reciprocal space which describes the effect of the longitudinal strain on the reciprocal lattice. It will be taken to point in the direction of the sound velocity and will have magnitude equal to the magnitude of the strain in the metal. Thus, the effect of a positive strain will be to increase the $\vec{\epsilon}$ component of any position vector in reciprocal space by a fraction ϵ. The $\vec{\epsilon}$ component of a vector $\vec{R}$ is given by $\vec{R}\cdot\vec{\epsilon}/\epsilon$, so the change in a vector $\vec{R}$ will be given by $\Delta\vec{R} = (\vec{R}\cdot\vec{\epsilon})\vec{\epsilon}/\epsilon$. The vectors $\vec{\mu}_i$, which represent the changes in position of reciprocal-lattice points, are then given by

$$\vec{\mu}_i = (\vec{L}_i\cdot\vec{\epsilon})\vec{\epsilon}/\epsilon , \quad (18)$$

where the $\vec{L}_i$ are the reciprocal-lattice points

$$\vec{L}_1 = (1,1,1), \quad \vec{L}_2 = (1,1,\bar{1}), \quad \vec{L}_3 = (2,0,0) . \quad (19)$$

Because they carry information about the changes in the pseudopotential coefficients with strain, the λ's are more difficult to calculate. If it is assumed that the pseudopotential coefficients depend only upon the distance between reciprocal-lattice points, it is clear that $V_{\vec{g}} = F(g)/\Omega$, where $\vec{g}$ is the vector connecting two reciprocal-lattice points, $F(g)$ is the corresponding form factor, and Ω is the atomic volume. With these simplifications, the λ_i are given by

$$\lambda_i = \frac{1}{\Omega}\left(\frac{\partial F(g)}{\partial g}\right)_{g_i} \Delta g_i + F(g_i)\frac{-1}{\Omega^2}\Delta\Omega , \quad (20)$$

where the vectors $\vec{g}_i$ are defined by the relations

$$\begin{aligned} &\vec{g}_1 = \vec{L}_1 - (0,0,0) = (1,1,1), \quad \vec{g}_4 = \vec{L}_2 - \vec{L}_1 = (0,0,\bar{2}) , \\ &\vec{g}_2 = \vec{L}_2 - (0,0,0) = (1,1,\bar{1}), \quad \vec{g}_5 = \vec{L}_3 - \vec{L}_1 = (1,\bar{1},1), \\ &\vec{g}_3 = \vec{L}_3 - (0,0,0) = (2,0,0), \quad \vec{g}_6 = \vec{L}_3 - \vec{L}_2 = (1,\bar{1},1), \end{aligned} \quad (21)$$

and Δg_i is the change in length of $\vec{g}_i$ under the strain. This can be calculated by first considering the vector change in $\vec{g}_i$, namely, $\Delta\vec{g}_i = (\vec{g}_i\cdot\vec{\epsilon})\vec{\epsilon}/\epsilon$. Since $\vec{g}_i$ is much larger than $\Delta\vec{g}_i$, the vector $\vec{g}_i + \Delta\vec{g}_i$ will be approximately parallel to $\vec{g}_i$. Thus, the

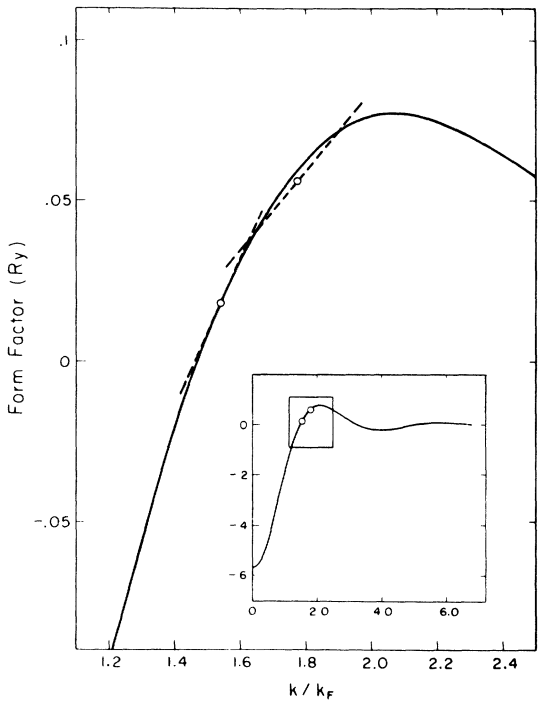

FIG. 11. Pseudopotential form factor for aluminum based on the model potential of Heine and Abarenkov. Circles are the Fourier coefficients determined by Ashcroft from the fit of a 4-OPW Fermi surface to dHvA data, and dashed lines through the circles are assumed slopes used in anisotropic model of the deformation parameter.

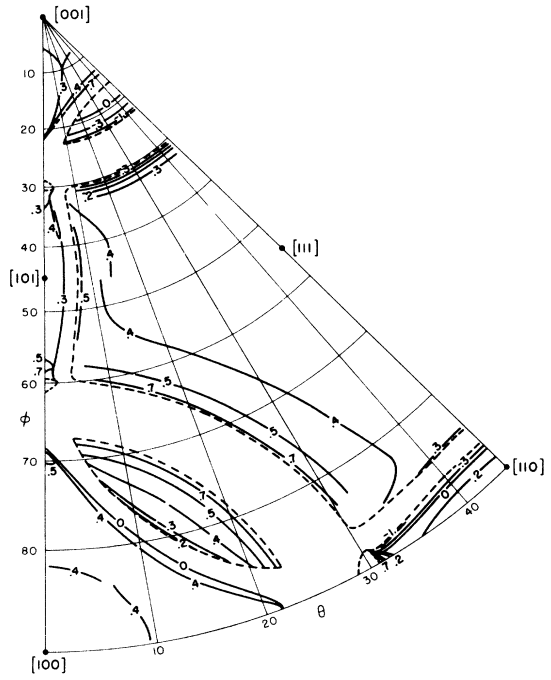

FIG. 12. Stereographic projection of curves of constant deformation on the extended-zone Fermi surface of aluminum for longitudinal [001] strain. Deformation, in units of $-2\pi/a$, is that calculated by the final anisotropic model. Pole of the projection is [001] and the intersection of the Fermi surface with the Brillouin zone is shown dashed. Breaks in the contours are due to truncation of the secular determinant to order four.

change in length of $\vec{g}_i$ will just be the $\vec{g}_i$ component of $\Delta\vec{g}_i$. This is given by $\Delta g_i = \Delta\vec{g}_i \cdot \vec{g}_i/g_i$ or

$$\Delta g_i = [(\vec{g}_i \cdot \vec{\epsilon})\vec{\epsilon}/\epsilon] \cdot \vec{g}_i/g_i = (\vec{\epsilon} \cdot \vec{g}_i)^2(1/\epsilon g_i) \ . \quad (22)$$

With $\vec{\epsilon}$ as defined above, the fractional change in the atomic volume is just the negative of ϵ, so that

$$\Delta\Omega = -\Omega\epsilon \ . \quad (23)$$

If $F(g)$ and $\partial F(g)/\partial g$ are known at $g=\sqrt{3}$ and 2, then all the λ_i for a given strain $\vec{\epsilon}$ can be calculated from Eqs. (20) and (22). The form factors $F(\sqrt{3})$ and $F(2)$ are given by ΩV_{111} and ΩV_{200}, respectively, while $\partial F(g)/\partial g$ can be obtained from the slope of the form factor for any one of several model pseudopotentials. The form factor of the model potential of Heine and Abarenkov,[18] a portion of which is shown in Fig. 11, was chosen because values are available in tabular form and because it gives coefficients V_{111} and V_{200} in close agreement with those determined empirically from a fit to dHvA data.[2] Finally, the parameter δ is chosen so that the Fermi surface of the strained metal has the proper volume. This is achieved by choosing δ to make the average deformation equal to the value previously calculated for the isotropic deformation.

The computer program to calculate the ultrasonic attenuation with this model deformation is similar to that used with the isotropic deformation, except that, at each point on the surface and for each propagation direction considered, the deformation is calculated by a subprogram. Since the calculation of the deformation greatly increases the duration of the program, only one principal propagation direction is considered for each computer run. Based on the slope of the Heine-Abarenkov form factor shown in Fig. 11, the values of $(1/\Omega)\partial F(g)/\partial g = 0.33$ and 0.15 are obtained for $g=\sqrt{3}$ and 2, respectively. These values of $(1/\Omega)\partial F(g)/\partial g$ give an average deformation of 0.3537 when δ is equal to 0.827ϵ. The change in sign of the deformation corresponds to the choice of a compression as a positive strain. Alternatively, the unit can be taken as $-2\pi/a$ with the usual definition of strain.

Measurements of the dHvA effect made under hydrostatic pressure have shown that the β and γ cross-sectional areas of the third-zone arms (see Fig. 7) change at the rates of 1.2 ± 0.15 and $-0.47 \pm 0.006\%$/kbar, respectively.[6] By comparison, the nearly-free-electron model would predict that both these cross sections should increase at the rate of 0.0745%/kbar. By taking the average deformation around these two cross sections for three mutually perpendicular linear strains, it is possible to calculate the expected change in area for an isotropic strain. With the volume compressibility of aluminum known from low-temperature elastic constants,[19] the change in area per unit pressure is given by

$$\frac{1}{A}\frac{dA}{dP} = \frac{\text{circumference} \times \text{average deformation} \times \text{compressibility}}{\text{cross-sectional area}} \ . \quad (24)$$

A computer program, using the model Fermi surface and the model deformation, has been written to perform the above calculations for the third-zone cross sections. The results are 1.35 and -0.43%/kbar for the β and γ cross sections, respectively.

Although these predictions are in good agreement with the experimental results, it was decided to vary the parameters of the anisotropic deformation model so as to obtain a perfect fit. Because it was felt that the low-pressure data[6] for the γ cross section could best be represented by a slope of -0.43%/kbar, it was not desired to change this value. For $(1/\Omega)\partial F(g)/\partial g = 0.307$ at $g=\sqrt{3}$ and 0.165 at $g=2$ (shown by dashed lines on Fig. 11),

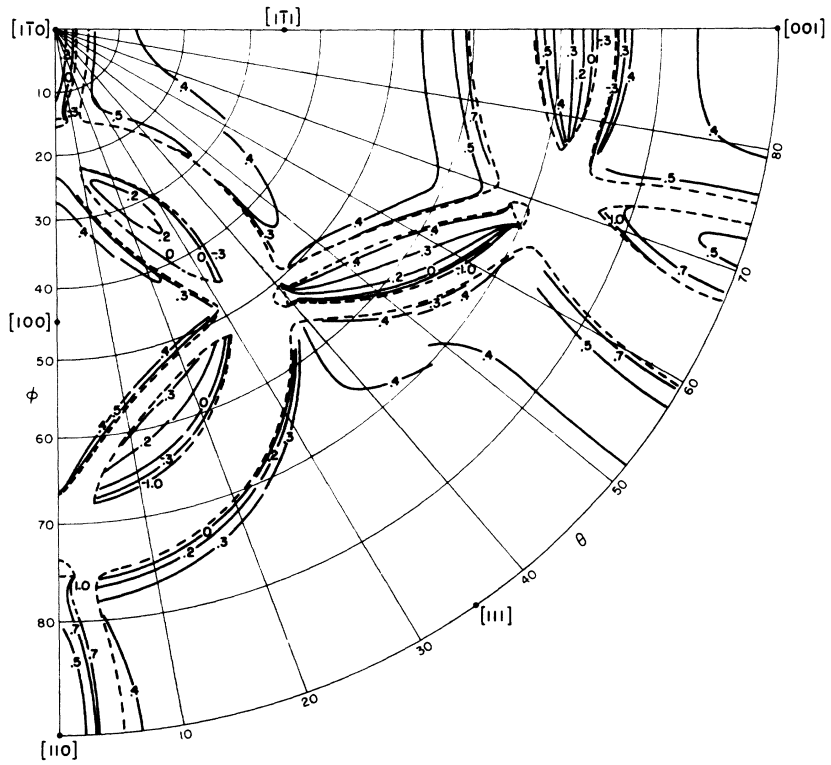

FIG. 13. Stereographic projection of curves of constant deformation on the extended-zone Fermi surface of aluminum for longitudinal [1Ī0] strain. The deformation, in units of $-2\pi/a$, is that calculated by the final anisotropic deformation model. Pole of the projection is [1Ī0] and the intersection of the Fermi surface with the Brillouin zone is shown dashed. Breaks in the contours are due to truncation of the secular determinant to order four.

perfect agreement is achieved with dHvA measurements. A slightly different δ of 0.826ϵ is then required to achieve charge conservation, giving $K_{av} = 0.3533$.

With these new parameters in the deformation model, the ultrasonic attenuation has been calculated assuming an isotropic mean free path. The results are shown by the solid lines on Figs. 3–5 and in Table IV. For [100] and [111] propagation, this deformation model provides a good fit to the data over the entire range of ql. Only for [110] propagation at high ql does the predicted attenuation fail to agree with experiment, and even here the results are clearly superior to those based on the free-electron or isotropic deformation models. Because values of α/f calculated with this deformation are relatively insensitive to changes in the parameters $(1/\Omega)\partial F(g)/\partial g$, it is unlikely that further changes in the latter could significantly improve the agreement. In Sec. IV B it was pointed out that, because of lack of perfect symmetry, the model Fermi surface is less satisfactory at high-ql values for calculations involving [110] propagation then the other directions. Although corrections have been applied for this lack of symmetry, it is difficult to estimate the remaining uncertainty in the computed behavior. It does not seem unreasonable, however, to ascribe the discrepancy between theory and experiment at $ql = 20$ to this source.

Table II shows the electron mean free paths required to fit the attenuation predicted by this model to the experimental data at low values of ql. Although the agreement of electron mean free paths in samples of the same purity is not especially good, it is within the experimental uncertainty of the measurements. The previous anisotropic deformation model provided slightly different values of electron mean path and α/f, but the over-all agreement was neither better nor worse.

Figures 12–14 show stereographic projections of curves of constant deformation, in units of $-2\pi/a$, for linear strains along the three principal symmetry axes. These figures, which were pieced together by considering $\frac{1}{48}$th of the Fermi surface for several propagation directions, show that the model deformation parameter lacks perfect symmetry to about the same extent as the model Fermi surface. It can be seen that the deformation parameter is relatively constant over most of the second-zone surface but varies strongly near its edges and over most of the third zone. Since the deformation enters through the pseudopotential, one would expect those parts of the Fermi surface most strongly influenced by the pseudopotential to have the strongest anisotropy of deformation, and this is just what is observed.

V. CONCLUSIONS

Measurements of the electronic contribution to the ultrasonic attenuation have been made over a

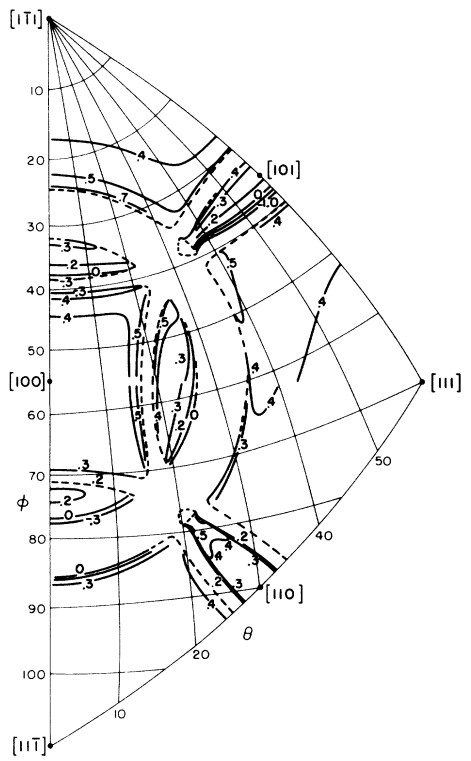

FIG. 14. Stereographic projection of curves of constant deformation on the extended-zone Fermi surface of aluminum for longitudinal [1$\bar{1}$1] strain. Deformation, in units of $-2\pi/a$, is that calculated by the final anisotropic model. Pole of the projection is [100] and the intersection of the Fermi surface with the Brillouin zone is shown dashed. Breaks in the contours are due to truncation of the secular determinant to order four.

wide range of ql for longitudinal waves propagating along the three principal symmetry directions in aluminum. Values of electronic attenuation divided by frequency are found to be linear in frequency for ql small and approximately constant for ql large. The limiting values of α/f at high ql are found to be highly anisotropic and not in agreement with the predictions of the free-electron model. Deviations of the Fermi surface from the free-electron sphere are found to have a strong influence on the electronic attenuation, but calculations made with an isotropic deformation parameter are still not in good agreement with experiment. Since there is no reason to believe that the Fermi surface model or the ultrasonic attenuation theory are seriously deficient, it seems certain that the deformation parameter must be anisotropic.

By considering the effect of a static longitudinal strain on the pseudopotential model of the Fermi surface, a deformation model with two independent parameters has been developed. This model deformation is found to give good agreement with the measured ultrasonic attenuation as well as with dHvA measurements made under hydrostatic pressure. Only for [110] propagation at high ql is the predicted attenuation not within the experimental error and, even in this case, the agreement between experiment and theory is significantly improved by the use of a model anisotropic deformation parameter.

Average values of electron mean free path, chosen to fit the calculations to the low-ql measurements, are not in very good agreement for different propagation directions in samples of the same purity. This would tend to indicate that the electron mean free path may not be isotropic as was assumed in the calculations. If a model for an anisotropic electron mean free path could be developed, it could be incorporated into the calculations and compared with experiment to test its validity.

Longitudinal measurements made at higher ql probably would not provide any better check on the deformation model. For [110] propagation, the lack of perfect symmetry of the Fermi-surface model severely limits the accuracy of high-ql calculations. As ql increases from 20 to 100, the present calculations would predict an increase in α/f of about 16% for [100] propagation and a decrease of about 3% for [111] propagation. Unless the uncertainty associated with the dislocation attenuation could be eliminated for [100] propagation, both of these trends would most likely be masked by experimental uncertainty. Best results for [100] propagation at very high ql would probably be obtained by making measurements on a thin very-high-purity sample below the transition temperature, where $\alpha_{\text{electronic}} = \alpha_n - \alpha_s$ as $T \to 0\,^{\circ}\text{K}$. A weak amplitude-dependent attenuation might be present in this region, but the results could be extrapolated to zero amplitude, as has been done in indium.[20]

Although measurements made for propagation along nonsymmetry directions would be interesting, the theoretical calculations would probably be too time consuming unless they were limited to the case of $ql \gg 1$. Probably the most promising project for future work would be to extend the same type of model deformation to the case of transverse waves. The same two-parameter model would apply, but the lattice and hence the Fermi surface would be distorted differently by the transverse strain. If such a deformation model should prove to accurately describe the experiments at high ql (where α/f is independent of l) for both longitudinal and transverse waves, then a reliable model for both the Fermi-surface shape and static deformation properties would be available.

It is felt that the results of this study support three general conclusions. First, measurement of the electronic contribution to the ultrasonic attenuation is a powerful tool for the investigation of

the low-wave-number electron-phonon interaction, especially in metals where the Fermi surface is well known. Second, nothing is found to indicate that the general theory of ultrasonic attenuation is not completely valid within its stated limitations. Finally, it appears that, as calculations of ultrasonic attenuation become more sophisticated, greater consideration must be given to the possibility of an anisotropic electron mean free path.

ACKNOWLEDGMENTS

Thanks are due to Dr. E. S. Bliss for much helpful advice and to S. K. Wang who measured the resistance ratios in the samples.

†Work supported by the NSF. Based on a thesis submitted by one of us (K. C. H.) as partial fulfillment of the requirements for the Ph. D. degree in physics at Carnegie-Mellon University.

*Present address: U. S. Naval Weapons Laboratory, Dahlgren, Va. 22448.

[1]A. B. Pippard, Proc. Roy. Soc. (London) A257, 165 (1960).
[2]N. W. Ashcroft, Phil. Mag. 8, 2055 (1963).
[3]H. David, H. R. Van der Laan, and N. J. Poulis, Physica 28, 330 (1962).
[4]B. Berre and T. Olsen, Phys. Status Solidi 11, 657 (1965).
[5]E. A. Fagen, thesis (University of Pittsburgh, 1967) (unpublished).
[6]V. D. Fil', O. A. Shevchenko, and P. A. Bezuglyi, Zh. Eksperim. i Teor. Fiz. 54, 413 (1968) [Sov. Phys. JETP 27, 223 (1968)].
[7]W. E. Timms, thesis (University of Lancaster, Lancaster, England, 1968) (unpublished).
[8]P. J. Melz, Phys. Rev. 152, 540 (1966).
[9]C. P. Bean, R. W. DeBlois, and L. B. Nesbitt, J. Appl. Phys. 30, 1976 (1959).
[10]T. E. Faber and A. B. Pippard, Proc. Roy. Soc. (London) A231, 336 (1955).
[11]R. E. MacFarlane and J. A. Rayne, Phys. Rev. 162, 532 (1967).
[12]A. Granato and K. Lücke, J. Appl. Phys. 27, 583 (1956).
[13]A. H. Wilson, *Theory of Metals* (Cambridge U. P., Cambridge, England, 1958).
[14]A. B. Pippard, Phil. Mag. 46, 1104 (1955).
[15]D. J. Meredith and J. A. Rayne (unpublished).
[16]W. A. Harrison, Phys. Rev. 116, 555 (1959).
[17]W. A. Harrison, Phys. Rev. 118, 1182 (1960).
[18]V. Heine and I. Abarenkov, Phil. Mag. 9, 451 (1964).
[19]G. N. Kamm and H. V. Bohm, Phys. Rev. 131, 111 (1963).
[20]E. S. Bliss and J. A. Rayne, Phys. Rev. 177, 673 (1969).

PHYSICAL REVIEW B VOLUME 4, NUMBER 4 15 AUGUST 1971

Electronic States as Linear Combinations of Muffin-Tin Orbitals

O. K. Andersen
H. C. Ørsted Institute, University of Copenhagen, Copenhagen, Denmark

and

R. V. Kasowski
Central Research Department E. I. du Pont de Nemours and Company, Experimental Station, Wilmington, Delaware* 19898

(Received 11 January 1971)

A general method for the calculation of electronic states in solids and molecules is proposed. As in the augmented-plane-wave scheme, we use the variational principle for the Hamiltonian in an energy-dependent basis. The basis functions, so-called muffin-tin orbitals, are generalizations of Heine's resonant orbitals. For a muffin-tin potential, the secular matrix has form $(1+\Lambda U)\Lambda$, where Λ is the matrix of the Korringa-Kohn-Rostoker (KKR) method and U is a simple matrix element of the potential. In contrast to the KKr scheme, the present method easily includes perturbations to the muffin-tin Hamiltonian.

I. INTRODUCTION

The scattered-wave—or Korringa, Kohn, Rostoker (KKR)—method has proved very useful for the calculation of electronic energy levels in solids[1] and molecules,[2] whenever the muffin-tin (MT) model is appropriate; that is, whenever the one-electron potential is spherically symmetrical inside nonintersecting atomic spheres and zero outside. For low energies and short-range potentials, the secular matrix is very small, since only partial waves $\psi_{lm}(E, \vec{r})$ of nonzero phase shift and of one energy contribute. Thus the radial quantum number n of the linear-combination-of-atomic-orbitals (LCAO) matrix does not appear, instead the KKR matrix depends implicitly on energy. Although the MT model describes the potential in close-packed metals fairly well, it is not satisfactory in more